Di-tert-butyl Disulfide as a Replacement for Hydrogen Sulfide in the Atomic Layer Deposition of Two-Dimensional Molybdenum Disulfide

Ian E. Campbell,[1] Aashi Gupta,[2] Pavlina Metaxa,[2] A. Arifutzzaman,[2] Tao Ma,[1] Paula Arellano,[1] Ray Duffy[2], Ageeth A. Bol[1]*

[1] The University of Michigan, Ann Arbor, Michigan, 48109, United States of America.

[2] Tyndall National Institute, University College Cork, Lee Maltings, Cork T12 R5CP, Ireland.

*Corresponding Author, aabol@umich.edu

ABSTRACT: Atomic layer deposition (ALD), with its precise process control and conformality, has recently gained interest for synthesizing transition metal sulfides like MoS_2, which have varied applications in low-dimensional electronics and electrocatalysts. Hydrogen sulfide (H_2S) has been used in many sulfide ALD processes, however, H_2S is a toxic gas that requires expensive containment and abatement measures for shipping, installation, and storage. Herein, we report a PEALD process capable of synthesizing MoS_2 without H_2S. This process utilizes a Mo precursor commonly used in ALD, hydrogen plasma, and di-tert-butyl disulfide (TBDS), which is a liquid that is significantly less hazardous and expensive than H_2S. It was found that the TBDS-based PEALD process results in layered, stoichiometric MoS_2 with limited contamination. The TBDS-based PEALD process was also analyzed via mass spectrometry to determine the mechanistic roles of each reactant. Apparently, H_2 plasma removes ligands from the chemisorbed Mo precursor which allows TBDS to sulfurize the top layer, producing H_2S and isobutene as byproducts. MoS_2 films deposited via the TBDS-based process possessed fewer yet taller out-of-plane growths and similar crystal grain diameter (~10 nm) and electrical resistivity (13.6 - 15.5 Ω.cm for 3 nm thick films) compared to films made with H_2S. Thus, the TBDS-based process is a suitable and safer alternative to the H_2S-based process for large-area synthesis of layered MoS_2.

INTRODUCTION

Atomic layer deposition (ALD) is a vapor-phase synthesis method that utilizes self-limiting surface chemistry[1] to deposit films, nanoparticles, and even single atoms[2,3] with excellent process control and conformality.[4] Since its discovery,[5,6] ALD has become an important tool for academic and industrial thin film processing. The number of ALD publications has accelerated significantly,[7] and the breadth of materials accessible via ALD has become quite expansive.[8,9]

Recently, researchers have focused on the synthesis of layered transition metal dichalcogenides (TMDs) via ALD due to the increasing relevance of these TMDs for electronic device fabrication as well as energy production and storage.[10] Notably, the application of layered TMDs in these fields is highly dependent on low temperature, large-area processes with enhanced conformality and process control like ALD.

Molybdenum sulfide (MoS_2) is one of the most studied layered TMDs; it has an indirect band gap as a bulk material and a direct band gap as a monolayer, enabling it to be used in low-dimensional, flexible, and transparent electronics.[11–13] ALD is becoming a popular method for synthesizing thin MoS_2 films, however, many current ALD processes synthesize MoS_2 using H_2S, [14–20] which is a toxic, flammable, and colorless gas[21] that is heavier than air and whose odor can become imperceptible to humans at lethal concentrations due to olfactory paralysis.[22] As of 2010, H_2S was responsible for the second largest number of fatal gas inhalation incidents in workplaces after carbon monoxide.[22] Furthermore, while acute exposure to high concentrations of H_2S is potentially lethal, chronic exposure to concentrations below 0.01 ppm can also lead to adverse health effects.[23] H_2S poses substantial safety risks but its use also necessitates the installation and maintenance of expensive containment and abatement measures like gas cylinders, dedicated coaxial tubing, and gas cabinets.

We report a PEALD process capable of synthesizing MoS_2 without H_2S. The process studied here utilizes a Mo precursor commonly used in ALD,[14–16,24,25] hydrogen plasma, and di-tert-butyl disulfide (TBDS). While TBDS is flammable and toxic, it is a liquid at standard temperature and pressure and has a vapor pressure of ~10 torr at ~87 °C.[26] Being a liquid and having a relatively low vapor pressure at and above delivery temperatures makes TBDS far less dangerous and easier to contain than H_2S in the event of a spill or leak. Nevertheless, TBDS has a

high enough vapor pressure that it can be delivered via vapor draw methods and can be installed on an ALD reactor without additional containment or abatement mechanisms. In fact, TBDS has been used in such a way to synthesize non-layered NiS_x via ALD.[27]

While MoS_2 has been synthesized via ALD using other non-H_2S sulfur precursors, most MoS_2 films synthesized with these precursor combinations suffer from contamination[28,29] or an amorphous structure,[30–32] and post-deposition processing is required to achieve high-quality MoS_2 for electronic applications. In fact, to the best of the authors' knowledge, the only published precursor combination capable of producing MoS_2 films without requiring post-processing steps utilized $Mo(CO)_6$ and diethyl disulfide with diethyl sulfide as an inhibitor. However, it is worth noting that this study still utilized post-deposition annealing to improve crystal quality of the as-deposited MoS_2.[33] Thus, replacing H_2S in the ALD of MoS_2 and other layered TMDs is an active research topic deserving of attention.

Herein, layered MoS_2 films made with TBDS and H_2S as sulfur precursors were compared and were found to be similar in terms of growth rate, surface roughness, composition, crystal structure, and electrical properties. This makes TBDS a safer and less expensive alternative to H_2S for the ALD of layered transition metal sulfides.

EXPERIMENTAL

ATOMIC LAYER DEPOSITION

All films were deposited in a Veeco Fiji G2 ALD reactor at a table temperature of 350 °C on thermally grown 300 nm SiO2/Si unless otherwise specified. Films made using hydrogen sulfide (H_2S) were synthesized using a two-step recipe wherein the substrate was exposed to 15 s of bis(t-butylimido) bis(dimethylamino) molybdenum ($(tBuN)_2(NMe_2)_2Mo$) (98 %, Strem) ,

which was heated to 50 °C, followed by a 15 s chamber purge, a 10 s plasma exposure, and, finally, another 15 s chamber purge. The plasma used for the H_2S process consisted of H_2S (2 sccm), H_2 (8 sccm), and Ar (40 sccm) and was powered by a 14.6 MHz RF plasma generator at 300 W. This plasma composition is based on our previous work on ALD of MoS_2.[14] Further description of the H_2S-based ALD process can be found in the Supporting Information.

Films made using di-tert-butyl disulfide (TBDS; Tokyo Chemical Industry, >97%) were synthesized via a three-step ALD process that used $(tBuN)_2(NMe_2)_2Mo$, H_2 plasma, then TBDS, as shown in Figure 1 below. The Mo precursor step in the TBDS-based process was the same as in the H_2S-based process. The plasma step in the TBDS-based process lasted 8 s and used 50

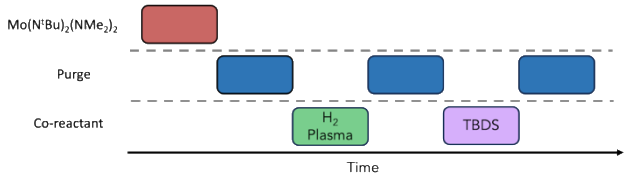

Figure 1. Schematic depicting the structure of the three-step, TBDS-based ALD process used to deposit MoS_2. The first and second purges are structured the same as the first and second purges of the two-step, H_2S-based process as described in the Supporting Information (Figure S 1). The third purge is 10 s long and occurs while rough pumping.

sccm of H_2 gas. The second purge was the same as in the H_2S-based process (Figure S1). The third step of the TBDS-based process was a 2 s dose of TBDS, which was heated to 55 °C, followed by a 10 s purge of the chamber using the roughing pump. Before every ALD process, SiO_2 substrates were loaded in the reaction chamber and cleaned with a 30 s O_2 plasma (50 sccm O_2 with 30 sccm Ar in carrier line, 300 W). The process chamber pressure was ~80 mTorr during rough pumping and ~8 mTorr during turbo pumping.

SPECTROSCOPIC ELLIPSOMETRY

In-situ spectroscopic ellipsometry (iSE) was performed using an M-2000 J. A. Woollam spectroscopic ellipsometer mounted onto the ALD process chamber at a 65.7 ° angle. The spectral range was 370 – 1000 nm. The fast acquisition mode (data collection every 0.5 s) was used to observe real-time saturation behavior of the reactants for recipe optimization, and the standard acquisition mode (data collection every 2 s) was used to measure the thicknesses of films made using the optimized recipe.

Saturation behavior for all reactants was modeled using the equation:

$$A(1 - e^{-t/T}) + (a * t),$$

where the surface saturating nature of the ALD reactions is accounted for by an exponential increase characterized by an amplitude, A, and a time constant, T. CVD-like reactions are also accounted for using a linear approximation where a is the slope. In both terms, t is the precursor or co-reactant exposure time.

TIME-DEPENDENT MASS SPECTROMETRY

Time dependent mass spectrometry was performed using a Hiden Analytical Limited HPR-30 Residual Gas Analyzer (RGA) equipped with oxide coated tungsten filaments and a 0.05 mm orifice for sampling the ALD process gases. The RGA was connected to the ALD reactor process chamber and line scans monitoring species having mass-charge ratios (M/Z) of 2, 16, 17, 18, 34, 40, and 56 were collected for the TBDS-based ALD process.

Since the sampling rate required for the RGA to measure reaction by-products was too slow to characterize standard ALD cycles, a stop-flow type ALD recipe was used to enable higher quality RGA measurements of the ALD process. Pumping of the process chamber was immediately stopped before Mo precursor and TBDS doses and the pressure in the process chamber was allowed to increase up to 2.7 Torr before pumping was resumed. Then, a 60 s

long purge was performed. Pumping of the process chamber was stopped immediately after the H_2 plasma dose to keep the plasma stable and a 60 s long purge was performed. Meanwhile, mass spectrometry measurements were acquired every 24 seconds.

ATOMIC FORCE MICROSCOPY

Atomic force microscopy (AFM) was performed using a Bruker Icon Atomic Force Microscope. The AFM instrument was operated in PeakForce Tapping mode with Scan Asyst-Air silicon nitride probes. AFM image processing was performed using Bruker Nanoscope Analysis software. Gradients in each AFM image were compensated using a first-order approximation. Film thicknesses were obtained by removing a portion of the as-deposited film by scratching with Delrin tweezers, acquiring an AFM image of the edge of the scratch, then vertically averaging the image to obtain a height profile of the scratch. Note that Raman spectroscopy was used to ensure that no MoS_2 vibrational modes were observed in the scratches.

RAMAN SPECTROSCOPY

Raman spectroscopy was typically performed on ~10 nm thick films. Raman spectra were acquired using a WiTec brand DPSS laser (30 mW, 532 nm), a UHTS 300 VIS-NIR spectrometer, and an alpha300R Access Mini confocal microscope equipped with a grating having 1800 lines per mm, a 50x objective, and a CCD detector. Raman spectra were analyzed in Origin software according to the methods used by Akhil *et al.*[14] and Mignuzzi *et al.*[34] and were calibrated to place the Si substrate peak at 520.6 cm^{-1}. Five Voight peaks were fit to the range between 330 and 430 cm^{-1} to model contributions from the TO(M), LO(M), E^1_{2g}, A_{1g}, and ZO(M) vibrational modes found in Raman spectra for disordered MoS_2.

X-RAY PHOTOELECTRON SPECTROSCOPY

X-Ray photoelectron spectroscopy (XPS) measurements were performed in a Kratos Axis Ultra instrument using monochromatic Al Kα X-rays and charge neutralization in the form of an electron flood gun. The emission current and anode voltage were set to 10 mA and 12 kV, respectively. Survey spectra were acquired using a pass energy of 100 eV and a resolution of 0.5 eV, while high resolution scans of specific elemental signatures (core spectra) were acquired with a pass energy of 20 eV and a resolution of 0.1 eV. All spectra were normalized with respect to binding energy to place the maximum intensity observed in the C 1s region at 284.5 eV. Angle-resolved XPS measurements (ARXPS) were performed by acquiring identical data sets at collection angles of 0, 55, and 75 °.

TRANSMISSION ELECTRON MICROSCOPY

For cross-sectional Transmission Electron Microscopy (TEM) observations, a JEOL 2100 TEM, operating at 200 kV and equipped with a double-tilt holder and a LaB 6 electron gun. Imaging was performed at 200kV. Interlayer spacing and film thickness values were measured manually in the Fiji image analysis software package.

Films examined via plan-view TEM were deposited directly on top of TEM grids Plan-view high-angle annular dark-field scanning transmission electron microscopy (HAADF-STEM) was performed on a Thermo Fisher Scientific Talos F200X S/TEM operated at 200 kV, with a probe convergence angle of 10.5 mrad. The collection range for the HAADF images is 56–200 mrad.

4P/2P HALL MEASUREMENTS

The 4-point and 2-point resistance (4P/2P) measurements were performed at room temperature using LakeShore HMS 8400 series instrument with both DC and AC measurement capabilities. A magnetic field reversal strength of ±1.7T was used for the DC measurements, and of $1.2T_{rms}$ for the AC measurements. Current reversal was performed to ensure minimal errors. Prior to all measurements, system calibration was verified using the two-geometry setups with the standard 1 cm × 1 cm InAs samples. MoS_2 on sapphire substrate was used for all the 4P and 2P measurements, to avoid the interference from the underlying Si substrate. The electrical measurements were taken at room temperature.

TEST STRUCTURE FABRICATION AND ELECTRICAL TESTING

Circular transfer length method (C-TLM) structures were patterned using optical lithography. A negative resist was used for this process. This was followed by the deposition of Ti/Au metal (10/150nm) using thermal evaporation. A standard liftoff process was employed to complete the fabrication process, with acetone as the liftoff solvent. The electrical measurements were performed at room temperature using an Agilent B1500A semiconductor device analyzer with a Cascade Microtech probe station.

RESULTS AND DISCUSSION

ALD PROCESS DEVELOPMENT

The durations required for each precursor dose to saturate the film's surface, or saturation times, were measured in real-time via iSE at a temperature of 350 °C. In real-time iSE measurements, the apparent change in film thickness was observed in 0.5 s increments and resulting data were fit with the model described in the methods above.

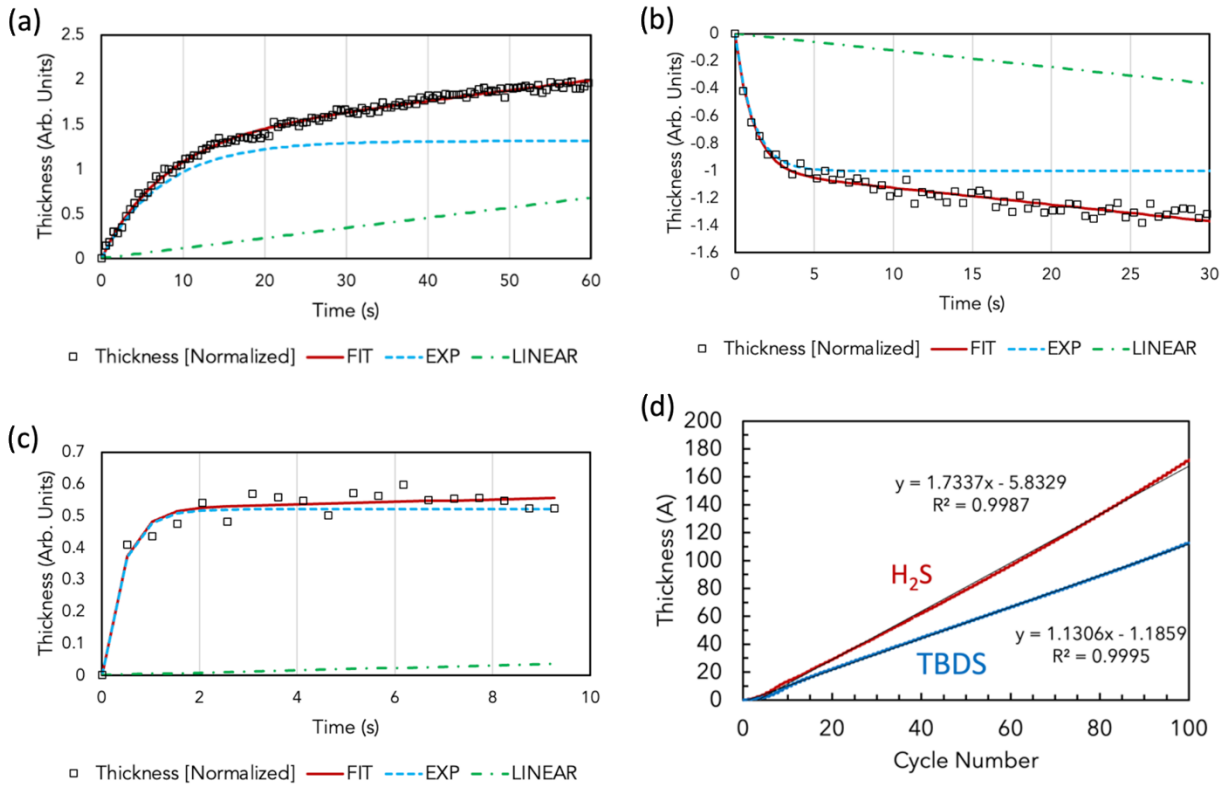

Figure 2. Change in apparent film thickness vs time, as recorded by iSE, resulting from: (a) a 60 s $(tBuN)_2(NMe_2)_2Mo$ dose in an ALD cycle also containing an 8 s H_2 plasma dose and a 2 s TBDS dose, (b) a 30 s H_2 plasma dose in an ALD cycle also containing a 15 s $(tBuN)_2(NMe_2)_2Mo$ dose and a 2 s TBDS dose, (c) a 2 s TBDS dose in an ALD cycle also containing a 15 s $(tBuN)_2(NMe_2)_2Mo$ dose and an 8 s H_2 plasma dose, and (d) change in film thickness vs number of ALD cycles for the TBDS and H_2S-based processes.

The $(tBuN)_2(NMe_2)_2Mo$ saturation curve shown in Figure 2a was collected from a recipe using a 60 s $(tBuN)_2(NMe_2)_2Mo$ dose, a 8 s H_2/Ar (10 sccm/40 sccm) plasma dose, and a 2 s TBDS dose. The exponential ALD component is plotted as a blue dashed line and the linear CVD component is plotted as a green line with alternating dashes. A dose time of 15 s was chosen for the $(tBuN)_2(NMe_2)_2Mo$ dose to balance maximizing the ALD component with minimizing the CVD component. The behavior of the $(tBuN)_2(NMe_2)_2Mo$ dose was very similar in the H_2S-based process so the same dose time of 15 s was chosen (Figure S2). With

the $(tBuN)_2(NMe_2)_2Mo$ and TBDS doses fixed at 15 and 2 s, respectively, the H_2 plasma showed saturating ALD behavior at 8 s (Figure 2b).

Initially, a two-step TBDS process was attempted wherein only alternating $(tBuN)_2(NMe_2)_2Mo$ and TBDS doses were used, but no observable thickness changes were recorded via iSE. Only after introducing an H_2 plasma exposure between the $(tBuN)_2(NMe_2)_2Mo$ and TBDS doses, was repeatable saturating growth observed. It may be that the imide and/or amide ligands present on the substrate surface after $(tBuN)_2(NMe_2)_2Mo$ exposure are unreactive with TBDS. In fact, the H_2 plasma resulted in a negative change in apparent film thickness, which indicates the removal of ligands from chemisorbed species derived from $(tBuN)_2(NMe_2)_2Mo$. It is also probable that the H_2 plasma is responsible for reducing Mo atoms in the precursor molecules from their 6+ oxidation states to 4+ oxidations states found in MoS_2.

The H_2 plasma also caused potential etching behavior, which was observed as a linear component in the model with negative slope. Thermal effects due to plasma exposure have been ruled out as a source of this linear decrease in apparent thickness since the thickness change is not reversed when the plasma exposure is ended.

Finally, the TBDS dose (Figure 2c) shows saturating ALD behavior with little to no concurrent CVD or etching while the $(tBuN)_2(Nme_2)_2Mo$ and H_2 plasma doses are fixed at 15 and 8 s, respectively. A dose time of 2 s was chosen for TBDS since the ALD component of the model is first saturated at that time. It seems likely that TBDS reacts with the substrate surface, which should be H-terminated due to the H_2 plasma exposure in the B-step, to produce isobutene vapor and surface-terminating thiol groups[27] that $(tBuN)_2(NMe_2)_2Mo$ can react with.

In fact, mass spectrometry data collected from a stop-flow version of the TBDS-based ALD process show periodic pressure spikes for chemical species with M/Z = 56, which corresponds with singly charged isobutene. These spikes appear during the Mo precursor and TBDS doses (Figure 3a) and indicate that isobutene is produced during these steps. Isobutene production is expected to occur at the substrate surface via intramolecular β-H transfer which allows for the creation of surface thiol groups [27] and enables the subsequent reaction of $(tBuN)_2(NMe_2)_2Mo$. However, isobutene production was not expected to appear during the Mo precursor dose. It may be that some isobutene physisorbed on the ALD reactor chamber walls and substrate surface and was displaced during the $(tBuN)_2(NMe_2)_2Mo$ dose. Interestingly, a species with M/Z = 34, which correlated with singly charged H_2S, was observed during the H_2 plasma and TBDS steps. The presence of H_2S during the H_2 plasma step indicates etching (removal of S) from the MoS_2 film as was observed in the iSE data. Although, H_2S released during the TBDS step likely has a different origin. If -H groups originating from the H_2 plasma step coexisted on the substrate surface with thiol groups created by the TBDS exposure, then it seems likely that these -H and -SH groups could combine to form H_2S during the TBDS exposure as shown in Figure 3b.

Real-time iSE data acquired in ~2 s increments were recorded for two films made with 100 ALD cycles using H_2S plasma and TBDS (Figure 2d). The resulting thickness value was 112 Å for 100 cycles of the TBDS process, indicating a growth-per-cycle (GPC) of 1.12 Å/cycle. The growth rate of the H_2S-based process was found to be ~1.72 Å/cycle by a similar method. The GPC of the TBDS-process as determined from the corresponding slope in Figure 2d was found to be ~1.13 Å/cycle, which is approximately equal to the GPC determined for the TBDS process from absolute thickness measurements. Measuring the GPC of the H_2S-

based process gives a GPC of ~1.73 Å/cycle. Thus, the iSE data indicates that the TBDS-based process is significantly slower than the H_2S-based process, however, both growth rates are relatively fast for ALD in general.

Growth rates were also measured via AFM by scratching each film made with 100 ALD cycles and measuring the height of the step at the edge of the scratch. The GPCs determined this way are 1.1 and 1.5 Å/cycle for the TBDS and H_2S-based processes/respectively. These values are comparable to the values measured using iSE.

Growth rates were investigated with respect to deposition temperature (Figure S4) and a maximum GPC was observed for the TBDS-based process at a deposition temperature of 350 °C. A notable decrease in GPC for deposition temperatures below 300 °C is likely attributable to lower reactivity of TBDS at these temperatures, which will be discussed later. The GPC at

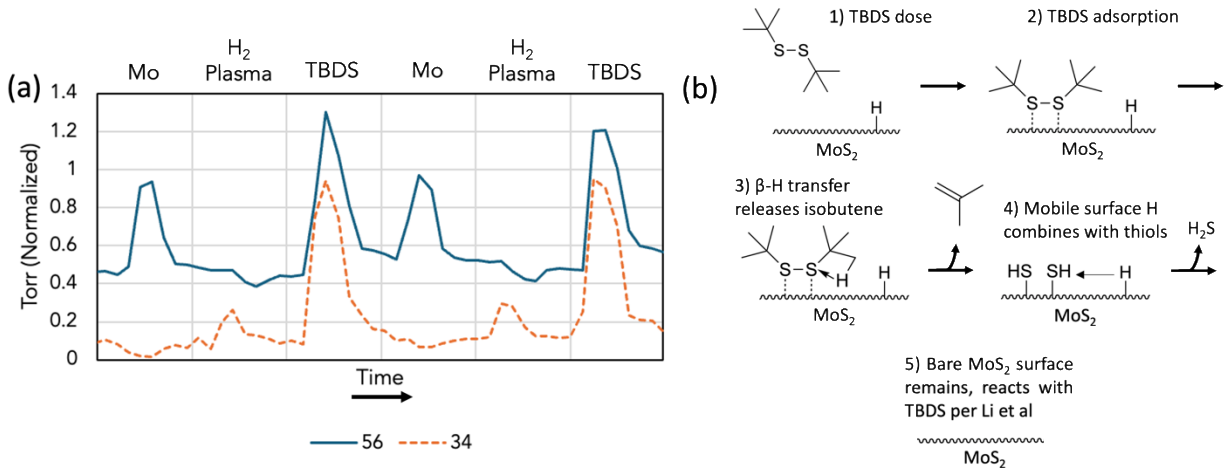

Figure 3. (a) Mass spectrometry line scan showing the prevalence of species exhibiting mass-charge ratios of 56 and 34 (M/Z = 56 and 34). Note the timeline has been segmented and labeled to illustrate which ALD step features in the line scan correspond with. Each labeled segment includes a stop-flow type dose and the subsequent purge. (b) Proposed mechanism for a reaction between TBDS and the MoS_2 substrate surface that results in isobutene (M/Z = 56) and H_2S (M/Z = 34) as byproducts.

450 °C is also significantly reduced compared to 350 °C, which may be due to desorption of

the $(tBuN)_2(NMe_2)_2Mo$ precursor leading to an undersaturated surface. The H_2S-based process exhibits the similar trends in GPC with respect to temperature as the TBDS-based process.

CHARACTERIZATION OF SURFACE ROUGHNESS

AFM analysis was performed on MoS_2 films deposited using the three-step TBDS process to characterize the films' roughness. 5 and 10 nm thick films were analyzed to study the relationship between film thickness and roughness The same analysis was performed on similar MoS_2 films made via the two-step H_2S-based ALD process.

An AFM image taken of a 5 nm thick MoS_2 film made using the three-step TBDS-based process is depicted in Figure 4a. Note the presence of vertical growths indicated by the lighter colors in the AFM image. These growths are most likely groups of MoS_2 layers that have grown out-of-plane with the substrate, resulting in fins (evidenced in TEM cross section images later). Fins are not uncommon when growing MoS_2 or other TMDs via vapor deposition methods.[10,14,15,19] Figure 4b is a histogram displaying the relative percent prevalence of height values for pixels from the AFM image in Figure 4a. The histogram in Figure 4b shows a slightly right-skewed peak centered around the arbitrary height of 0 nm, which corresponds to the height of the film where no fins have

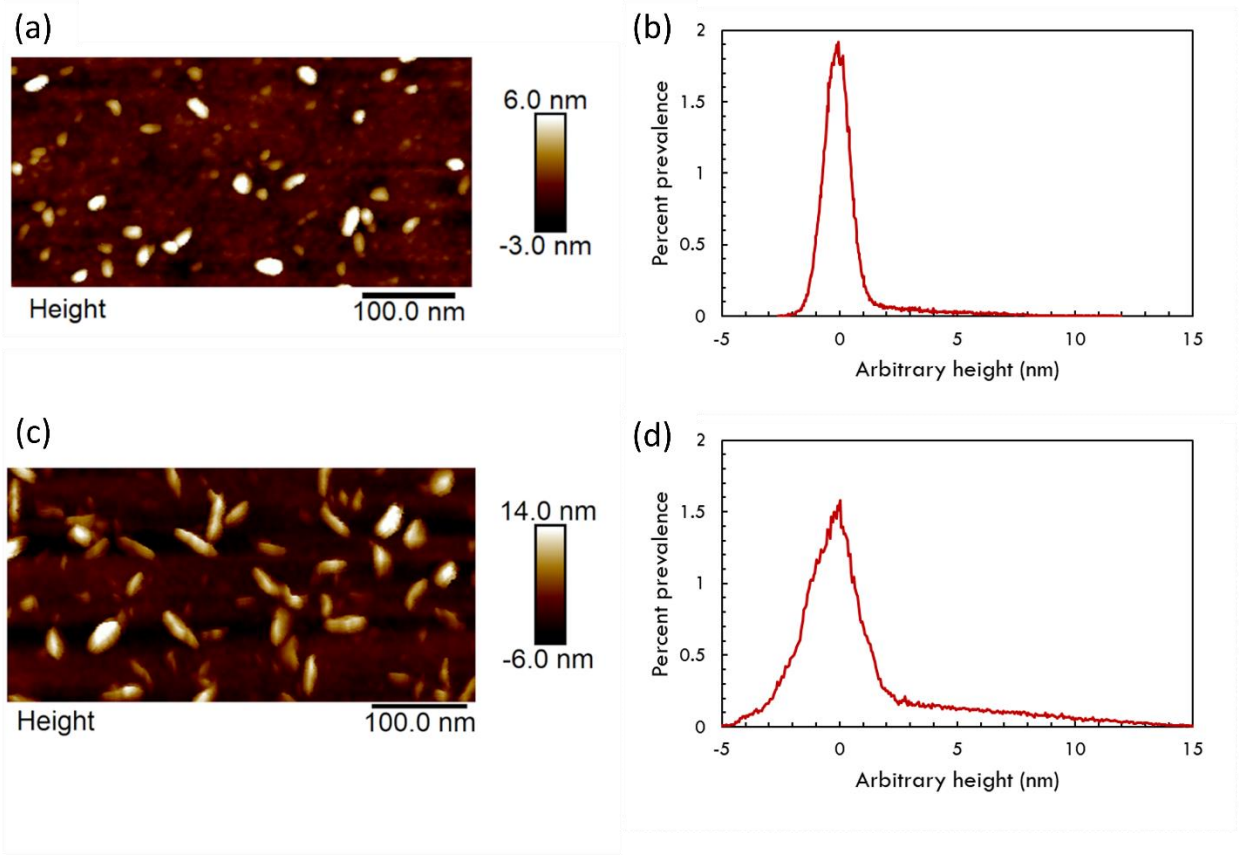

Figure 4. (a) AFM image of a 5 nm thick MoS_2 film deposited using the three-step TBDS process. (b) Height histogram displaying the relative percent prevalence of pixels in image (a) having a specific arbitrary height. (c) AFM image of a 10 nm thick MoS_2 film deposited using the three-step TBDS process. (d) Height histogram displaying the relative percent prevalence of pixels in image (c) having a specific arbitrary height.

grown. The slight skewing of this peak towards greater heights likely results from the small number of fins, which have heights greater than the rest of the film.

AFM analysis shows that a 10 nm MoS_2 film (Figure 4c) made using TBSD has noticeably larger and more plentiful out-of-plane fins than the 5 nm film. It seems fins continually appear and grow as the ALD process continues. The height histogram corresponding to the 10 nm film (Figure 4d) shows a relative increase in intensity for the right-skewed tail, also indicating the growth and appearance of new fins. The peak centered around 0 nm has broadened notably, which could be due to an increase in surface roughness for the parts of the film where no fins exist. The total range in height (Z_{range}), which may also be thought of as the maximum vertical peak-to-valley distance, as measured by AFM for Figure 4a is 17.7 nm, while Z_{range} for Figure 4c is 27.1 nm. An increase in Z_{range} as the deposition proceeds indicates that the fins grow in height as the ALD process continues.

A similar analysis was performed using AFM for films synthesized using the two-step H_2S process. An AFM image depicting a 5 nm thick MoS_2 film made using the two-step H_2S process is shown in Figure 5a. Comparing AFM images for the two 5 nm thick films (Figure 4a and Figure 5a) reveals that MoS_2 films made with H_2S have many more fins than those made with TBDS, although fins on MoS_2 made with H_2S appear smaller in height.

The height histogram corresponding to Figure 5 a (Figure 5b) shows a prominent shoulder on the peak centered around 0 nm. This shoulder appears with significantly greater intensity than the right-skewed tail in the histogram corresponding to the 5 nm thick film made with TBDS (Figure 4b), clearly demonstrating the presence of more fins on the film made with H_2S. Additionally, Z_{range} for the 5 nm thick film made with H_2S is 11.3 nm, which is significantly less than the Z_{range} observed for the corresponding film made with TBDS.

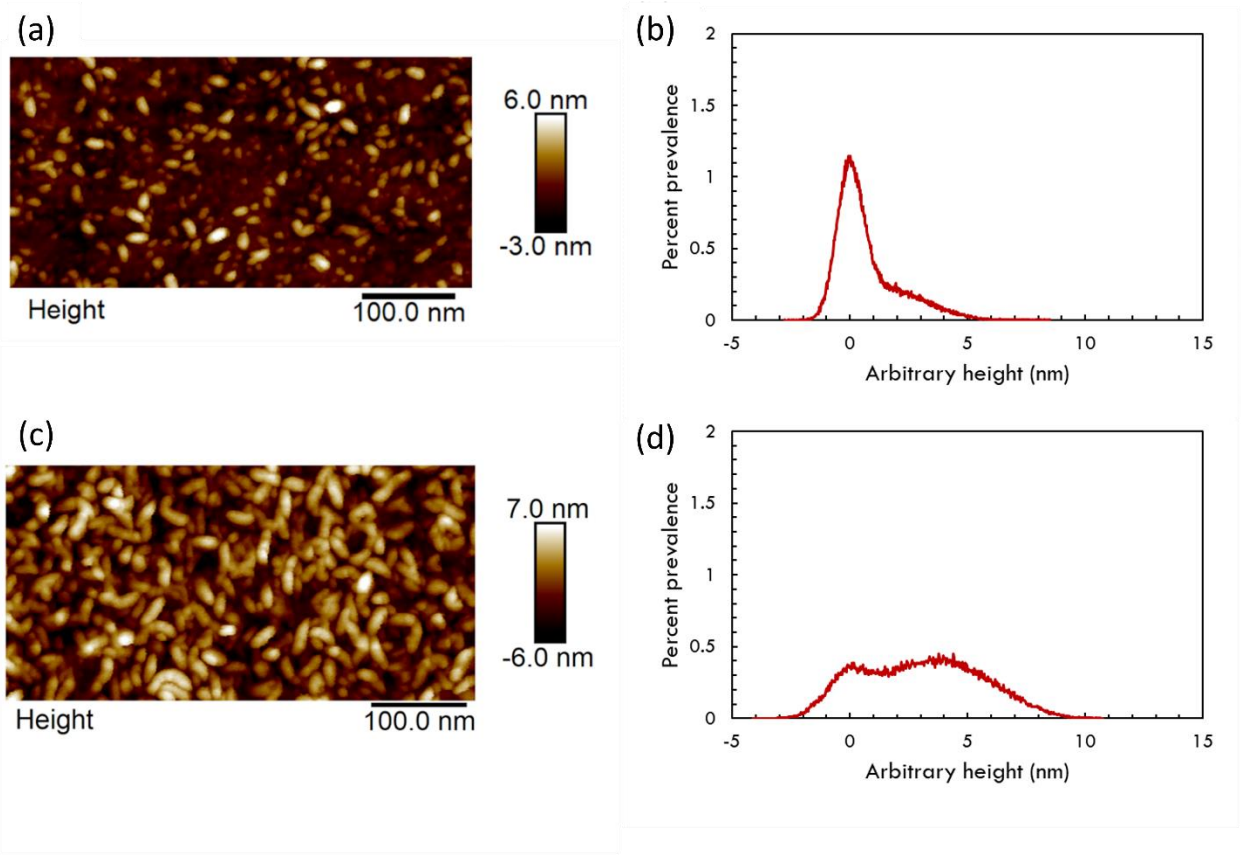

Figure 5. (a) AFM image of a 5 nm thick MoS_2 film deposited using the two-step H_2S process. (b) Height histogram displaying the relative percent prevalence of pixels in image (a) having a specific arbitrary height. (c) AFM image of a 10 nm thick MoS_2 film deposited using the two-step H_2S process. (d) Height histogram displaying the relative percent prevalence of pixels in image (c) having a specific arbitrary height.

An AFM image taken of a 10 nm thick film made with H_2S is displayed in Figure 5 c. In the height histogram corresponding to the 10 nm thick film made with H_2S, the shoulder associated

with fin growth now appears as a peak with greater percent prevalence than the peak centered around 0 nm. Thus, it could be said that a majority of the surface of the 10 nm thick film made with H_2S is covered with fins, whereas the 10 nm thick film made with TBDS is predominantly free of fins. Z_{range} for the 10 nm thick film made with H_2S is 14.9 nm, showing that fins do grow in height during the H_2S-based process, but they remain smaller than the fins observed on films made with the TBDS-based process.

CHARACTERIZATION OF COMPOSITION AND STRUCTURE

The acquired Raman spectra are shown in Figure 6. Figure 6a depicts a cropped Raman spectra taken of a ~10 nm thick MoS_2 film deposited using H_2 plasma and TBDS. Note the appearance of E^1_{2g} and A_{1g} Raman peaks at 382 and 407 cm^{-1}, respectively, which are characteristic of the in-plane and out-of-plane vibrational modes of multilayer 2H-MoS_2.[35,36] Figure 6b depicts a similar Raman spectrum acquired for a ~10 nm MoS_2 film made with H_2S-based plasma. Peak positions of 383.8 (E^1_{2g}) and 408 (A_{1g}) cm^{-1} were measured for this film. The slightly smaller separation between the E^1_{2g} and A_{1g} Raman modes for the film made with H_2S can be attributed to lower strain or doping as has been observed for MoS_2,[37,38] especially since the films characterized here are approximately the same thickness meaning effects of film thickness on this peak separation can be ruled out. Additionally, the defect-related transverse optical (TO(M)), longitudinal optical (LO(M)), and longitudinal acoustic (LA(M)) modes appear with greater intensity relative to the A_{1g} mode in the spectrum acquired for the film made with H_2 plasma and TBDS, indicating that the TBDS-based process introduces more defects into the MoS_2 structure than the H_2S-based process. All peak positions, areas, full widths at half-max, and the associated errors are reported in Table S 1.

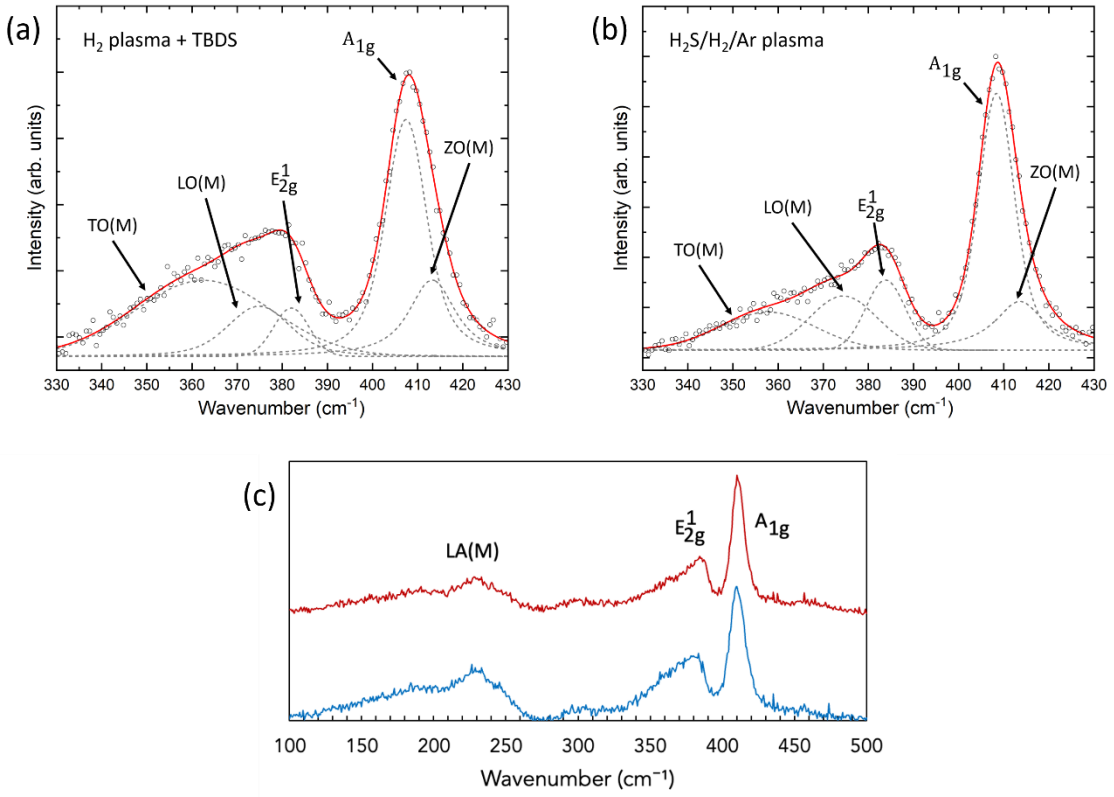

Figure 6. Deconvoluted Raman spectrum of a ~10 nm thick MoS_2 film deposited using: (a) a H_2S plasma and (b) a H_2 plasma and TBDS. Peaks attributed to E^1_{2g} and A^1_{1g} vibrational modes are characteristic of MoS_2 and those attributed to TO(M), LO(M), ZO(M), and LA(M) modes are all defect-related. (c) Raman spectra for ~10 nm thick MoS_2 films deposited using H_2S plasma (top, red) and H_2 plasma with TBDS (blue, bottom).

Raman spectroscopy was also used to characterize MoS_2 films grown via the TBDS-based process (100 ALD cycles) at deposition temperatures ranging from 150 to 450 °C (Figure 7). Note the appearance of the E^1_{2g} and A_{1g} modes in each spectrum acquired from films grown at deposition temperatures above 200 °C. Interestingly, these vibrational modes are missing from the spectra acquired from films synthesized at 200 °C and below. Apparently, TBDS is incapable of reacting to form MoS_2 at these temperatures and, presumably, MoC_xN_y is deposited as has been observed for $(tBuN)_2(NMe_2)_2Mo$ exposures alternated with H_2-based plasmas.[39,40]

An XPS core spectrum taken of the Mo3d and S 2s region at a collection angle of 0° for a 10 nm thick film made with TBDS is shown in Figure 8 a. The more intense doublet in the Mo3d data set possesses a peak separation of 3.14 eV, which is consistent with the peak separation attributed to spin-orbit splitting for the Mo3d signature of MoS_2.[41] The smaller doublet observed at higher binding energies in the Mo 3d core spectrum is attributed to the formation of a MoS_xO_y layer on the surface of the film due to air exposure that occurred while transferring the films from the ALD reactor to the XPS instrument. The Mo 3d XPS spectrum taken of the film made with TBDS closely resembles that taken from the film made with H_2S (Figure S7). The peak separation of the Mo 3d doublet for the film made with H_2S was also found to be 3.14 eV and the separation between the Mo 3d5/2 peak and the S 2s peak is 2.75 and 2.77 eV for the TBDS and H_2S plasma processes, respectively. Similar energy differences between the Mo3d5/2 and S 2s peaks imply similar chemical environments for Mo and S in each film.

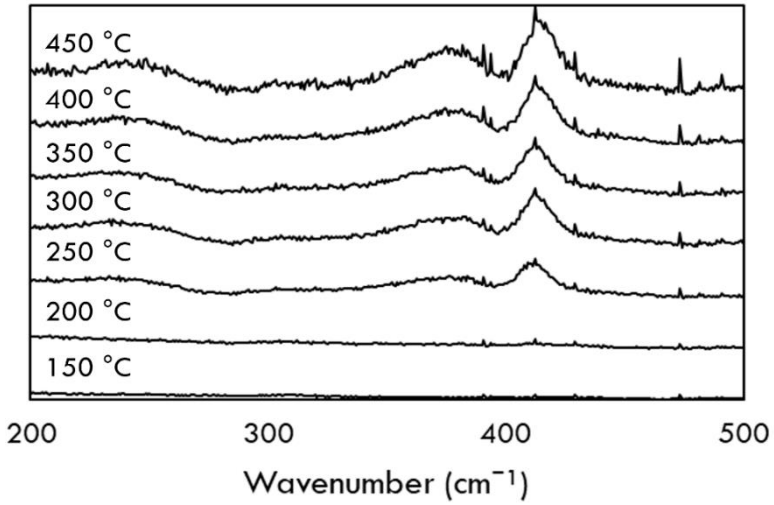

Figure 7. Raman spectra acquired from MoS_2 films synthesized using 100 cycles of the TBDS-based ALD process. Each spectrum is normalized to the maximum of the Si substrate signal at 520.6 cm^{-1}.

The S 2p XPS dataset taken from the film made with TBDS (Figure 8b) is best fit with two doublets, one lower in intensity and shifted to higher binding energies, indicating the presence of oxidized S species, which could also be attributed to a MoS_xO_y surface layer. The S:Mo ratio was calculated from these XPS data by dividing the total area of both S 2p doublets by the total area of Mo 3d doublets after adjusting each for their relative sensitivities. A S:Mo ratio of 1.98 was

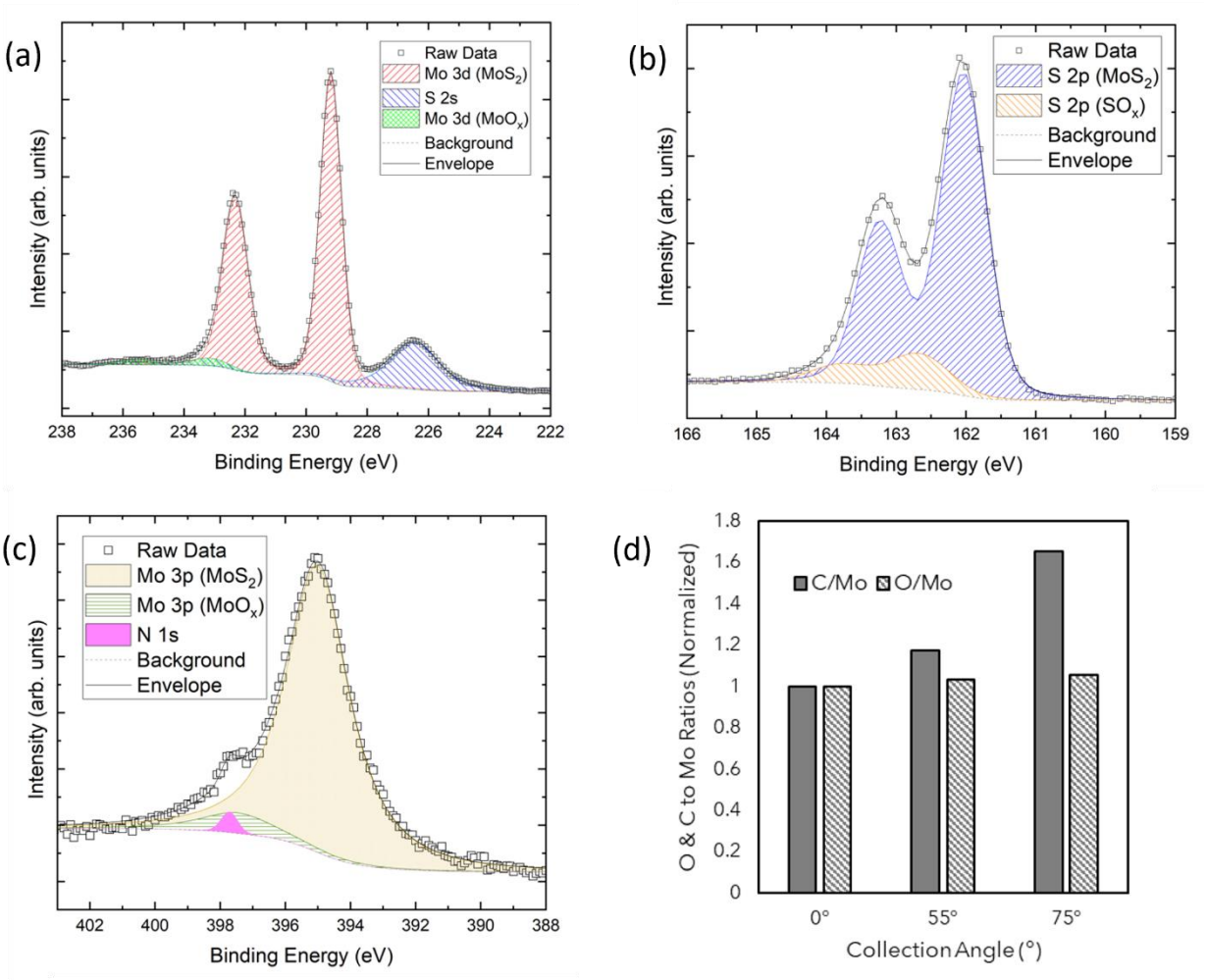

Figure 8. XPS data acquired from a ~10 nm thick MoS_2 film made with the two-step TBDS-based process. (a) Fitted XPS spectrum of the Mo3d and S 2s regions. (b) Fitted XPS spectrum of the S 2p region. (c) Fitted XPS spectrum of the Mo 3p 5/2 and N 1s regions. (d) Relative areas of peaks fit to XPS spectra featuring the C 1s and O 1s regions. The C 1s and O 1s regions were normalized for each film so that the peak areas for spectra collected at an angle of 0° are equal to 1 relative to the corresponding Mo 3d signal.

calculated for the film made with TBDS, indicating that the film possesses stoichiometry very close to MoS_2. A similar S 2p spectrum was acquired from the film made with H_2S (Figure S7), which yielded a S:Mo ratio of 1.96, indicating that both ALD processes are capable of synthesizing stoichiometric, or near stoichiometric, MoS_2. Additionally, the difference in binding energy between the Mo 3d5/2 and S 2p3/2 peaks for both types of MoS_2 was ~67.2 eV, which has been found to correlate strongly with a S:Mo ratio near 2:1.[42]

XPS was also used to evaluate the concentration of potential nitrogen, carbon, and oxygen contamination. Since the second step in each ALD process is a hydrogen-rich plasma, it is likely that the ligands on the Mo precursor are fragmented, which could allow for the incorporation of nitrogen or carbon from the tert-butyl imido or dimethyl amino groups. An N 1s core XPS spectrum was collected for the film made with TBDS (Figure 8c) to investigate the extent of nitrogen contamination. The N 1s spectrum also contained peaks corresponding to the Mo 3p3/2 signature due to spectral overlap. The larger Mo 3p3/2 peak is expected to originate from the bulk of the film, which is MoS_2, and the weaker Mo 3p3/2 peak is from the MoS_xO_y surface layer. To aid the deconvolution of this spectrum, the area of the MoS_xO_y Mo 3p3/2 peak was fixed relative to the MoS_2 3p3/2 peak in the same ratio as was found for the areas of the MoS_xO_y and MoS_2 doublets in the Mo 3d region. Comparing the areas of the N 1s peak and Mo 3d doublets indicates that the N:Mo ratio is 0.026 for the film made with TBDS. Interestingly, the N:Mo ratio calculated for the film made with H_2S was found to be 0.081. Thus, it is expected that the pure H_2 plasma used in the TBDS process is more efficient at removing the precursor ligands and their fragments from the film.

C 1s core spectra were taken at collection angles of 0°, 55°, and 75° to evaluate carbon contamination and to evaluate whether the C 1s signatures originate from adventitious carbon or

the interior of the MoS_2 films. While depth profile sputtering could be used, MoS_2 is known to experience preferential sputtering, which could complicate the calculation of stoichiometric ratios.[42] The XPS instrument used in this work is not equipped with a gas-cluster ion beam, which is recommended for samples sensitive to a regular argon ion beam. Thus, the C 1s signal was investigated via angle resolved XPS. Collecting XPS spectra at increasingly large collection angles yields compositional data from increasingly shallow sample depths.[43] By comparing a series of XPS signatures observed at various collection angles, it is possible to tell if a species is predominantly present on the surface or in the bulk of a film.

The recorded C 1s signature was able to be fit with a single peak. C/Mo ratios were calculated for the film by dividing the total area of the C 1s peak by the total area of the MoS_2 and MoS_xO_y doublets in the Mo 3d region at each collection angle. These ratios (Figure 8d) were then normalized with respect to each other to make the C/Mo ratio equal to 1 for each film at a collection angle of 0°. Note how the C/Mo ratio increases with increasing collection angle. Thus, the signal observed in the C 1s region has been attributed to adventitious carbon bound only to the surface of the film. Since the film made with H_2S yielded similar data for the C 1s region (Figure S7), it has been concluded that the C 1s signal obtained from films made with H_2S is also attributable to adventitious carbon.

O 1s/Mo 3d ratios were calculated in a similar fashion to the C 1s/Mo 3d ratios. The O 1s region consistently yielded weak signal that was difficult to reliably peak fit. Thus, the entire area beneath the raw data in the O 1s core scans was used, meaning that the signal was not deconvoluted to distinguish between oxygen on the surface of the films and oxygen within the films. However, comparing these ratios at different collection angles can indicate whether most of the oxygen is found at the surface or inside the films. Interestingly, the O 1s / Mo 3d ratio collected for the

TBDS-based film increases slightly with collection angle while the O 1s / Mo 3d ratio collected for the H_2S-based film decreases noticeably (Figure S7). Therefore, it is concluded that the H_2S-based film contains more oxygen than the TBDS-based film, which could be due to the reducing/etching nature of the H_2 plasma B-step used in the TBDS-based recipe.

Cross-sectional bright-field TEM (BF-TEM) analysis was performed on a ~10 nm thick MoS_2 film made with TBDS. Note that these films were deposited on thermally grown 90nm thick SiO_2/Si. A cross-sectional view of the MoS_2 and protective carbon and platinum layers is shown in Figure 9a. The relatively thin and dark layer in Figure 9a is the MoS_2 film as indicated by the labels and arrows. Figure 9b depicts a more magnified view of the MoS_2 film made with TBDS and reveals prominent horizontal striations with spacings of 0.66±0.05 nm, indicating that these alternating light and dark features are consistent with interlayer spacing in chemical vapor deposited MoS_2.[44] The film thickness as determined from cross-sectional BF-TEM images was found to be 8.5±0.4 nm. Note that these measurements were made where the films possessed no observable out-of-plane growth and that this thickness value is noticeably lower than those obtained via iSE and AFM. Since AFM and iSE take into account an "average" film thickness measured over a relatively large area and BF-TEM was used to differentiate between nanoscale areas with and without out-of-plane growth, it seems likely that out-of-plane growth has contributed to the larger film thicknesses observed from iSE and AFM. Cross sectional BF-TEM of a ~10 nm thick MoS_2 film made with H_2S reveals interlayer van der Waals gaps with similar spacing (0.66±0.04) and a film thickness of 7.6±0.6 nm.

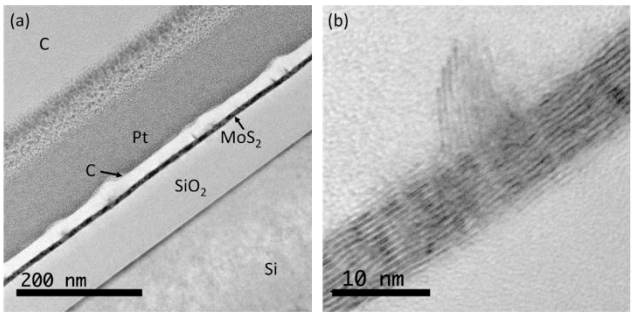

Figure 9. (a) Larger scale cross-sectional view of a ~10 nm thick MoS2 film deposited using TBDS on a 90 nm SiO2 layer on a Si wafer. (b) Magnified view of a ~10 nm thick MoS2 film. The protective carbon and platinum layers are visible in the larger scale micrograph.

Plan-view HAADF-STEM was also used to characterize the crystal grain structure of 5 nm thick MoS_2 films. A plan-view HAADF-STEM image taken of a film made with TBDS is shown below in Figure 10a with the corresponding FFT in the inset. The plan-view HAADF-STEM image shows a mottled light and dark gray regions, which do not appear to correspond with crystal grains as there are no obvious lattice fringes with the notable exception of the bright feature in the lower left portion of the image. This feature possesses alternating light and dark striations consistent with the interlayer MoS_2 spacing, meaning it is an out-of-plane fin-like growth. Despite the lack of obvious lattice fringes in the plan-view HAADF-STEM image, a ring of spots (highlighted in a blue arc) and a pair of spots with a smaller reciprocal spacing (highlighted in a yellow circle) are apparent in the FFT in the inset of Figure 10a. The rings correspond to a crystallographic spacing of ~0.27 nm, while the spots correspond to a spacing of 0.61-70 nm. These spacings are approximate due to the diffuse nature of the features in the FFT, but they agree well with published values for MoS_2 synthesized by ALD and CVD.[44,45] The ring in each pattern likely results from the $\{1\bar{1}00\}$ planes, which have spacings of 0.27 nm. The spots can be attributed to the (0001) planes, which delineate interlayer spacing of MoS_2.

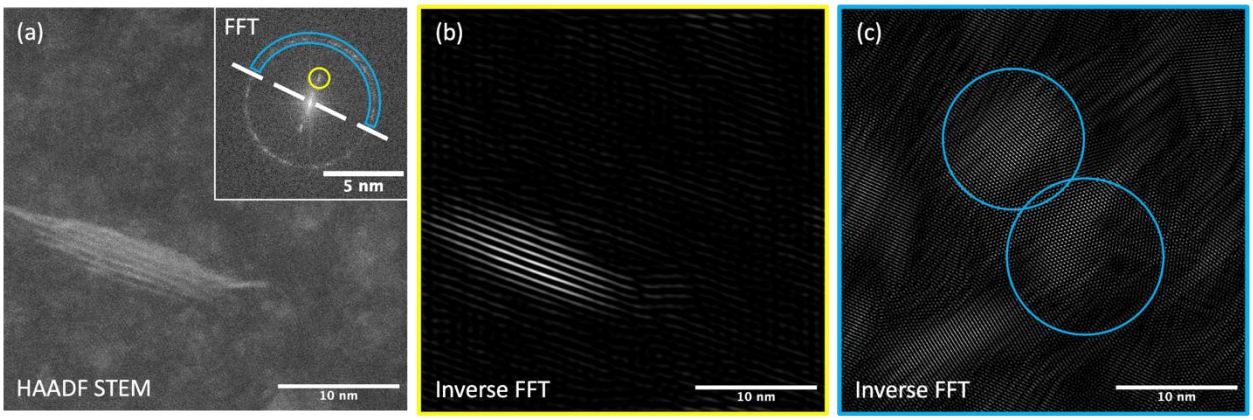

Figure 10. (a) Plan-view HAADF-STEM image depicting a 5 nm thick MoS_2 film deposited using TBDS on a 10 nm thick silicon nitride TEM window membrane previously coated with 5 nm of atomic layer deposited SiO_2; the inset depicts the corresponding FFT. (b) An inverse FFT constructed from the spot contained in the yellow circle in the inset in (a), note the presence of lattice fringes consistent with interlayer spacing in MoS_2. (c) An inverse FFT constructed from the spots contained in the blue arc in the inset in (a), note the lighter regions ~10 nm in diameter, some of which are indicated by circles.

Figure 10b and c are inverse FFTs constructed from the spots and the ring in the inset of Figure 10a, respectively. Note that the inverse FFT constructed from the spots highlights the position and structure of the fin, while the inverse FFT constructed from the ring highlights in-plane regions of the MoS_2 film. These regions of the MoS_2 film, which are approximately 10 nm in size, can be presumed to contain MoS_2 crystals that contain the information represented as the ring in the FFT. Thus, the crystal grain size is reported as 10 nm for the film made with TBDS. The same conclusion can be drawn from Figure S 9, which is the result of a similar analysis for the film made with H_2S. The bright regions in the inverse FFTs associated with crystal grains in each film can be observed more clearly in a series of inverse FFTs constructed from individual spots in the ring associated with the $\{1\bar{1}00\}$ planes (Figure S10 and Figure S11). It should also be noted that the lighter regions in the inverse FFT corresponding with in-plane crystal grain can be constructed and observed from multiple plan-view HAADF-STEM images acquired from various

regions of each type of film (Figure S12 and Figure S13), indicating that the grain size is ~10 nm across the entirety of the film.

Electrical resistivity was measured for MoS_2 films deposited using 100 cycles of the TBDS and H_2S-based ALD processes at deposition temperatures ranging from 150 to 450 °C (Figure 11). Note the jump in resistivity for the TBDS process as the deposition temperature increases from 200 to 250 °C. This sharp increase in resistivity corresponds with the appearance of MoS_2-related Raman modes upon increasing the deposition temperature from 200 to 250 °C. The resistivities found here for films deposited using the TBDS-based process at deposition temperatures below 250 °C are comparable to those reported in the literature for MoC_xN_y synthesized by ALD,[39] which could form if the TBDS were not reactive below 250 °C. In fact, the recipe used by Bertuch et al. utilizes the same Mo precursor with hydrogen-containing plasmas, meaning the TBDS-based MoS_2 process would effectively become the same as the MoC_xN_y process if TBDS becomes unreactive at temperatures below 250 °C. For deposition temperatures at and above 250 °C, the TBDS-based process synthesizes films with relatively consistent resistivities ranging from 0.04 – 0.08 Ω cm, exhibiting a slight positive linear trend with respect to increasing deposition temperature. It should be noted that the resistivities reported here are similar to, but somewhat lower than, those reported for atomic layer deposited MoS_2 elsewhere.[15]

Interestingly, resistivities recorded for the H_2S-based process exhibit an opposite trend with respect to deposition temperature, with higher resistivities occurring at lower deposition temperatures and a relatively strong negative correlation with respect to deposition temperature beginning at 250 °C (2.2 Ω cm at 250 °C and 0.003 Ω cm at 450 °C). While the decrease in resistivity with increasing deposition temperature for the H_2S-based process may be expected due to an overall increase in crystalline order, it is unclear why the resistivity of MoS_2 films made with

the TBDS process exhibit an opposing trend across the same range of deposition temperatures. The effects of deposition temperature and process type on charge carrier type and density will be investigated in future work to elucidate the origin of these effects.

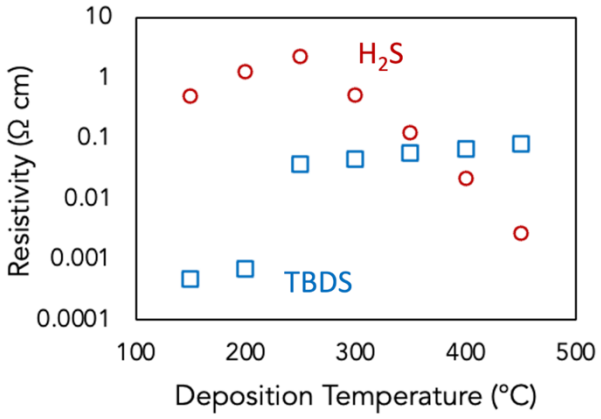

Figure 11. Resistivity measurements acquired from MoS_2 films made with 100 cycles of the TBDS and H_2S-based ALD processes at deposition temperatures ranging from 150 to 450 °C.

While the principal aim of this study is the exploration of MoS_2 synthesis methods using the TBDS precursor, electrical characterization is an important metrology method to understand the properties of resulting thin-film material. The objective of performing Hall and C-TLM measurements is to validate TBDS-synthesized MoS_2 in terms of conductivity, which is a fundamental pre-requisite for electron device operation. The subtle details of current transport and modulation will require a more detailed device-focused study, in terms of field-effect-transistor fabrication, with dimensions in the sub-micron regime. Nevertheless, demonstrating conductivity in TBDS MoS_2 thin-films is an important step-forward for this material system, as well as contrasting it with similar measurements performed on other MoS_2 thin-films, that are synthesized by other chemistries. The following electrical work is discussed in terms of the resistivity figure-of-merit. The deposition temperature for these films was 350 °C. The electrical measurements were all taken at room temperature.

Hall DC measurements were performed on 1 cm × 1 cm MoS_2 (3 nm thick) samples deposited on sapphire, using TBDS as the sulfur precursor. The 2-point (2P) measurements showed consistent ohmic behavior across all two-point contacts as presented in Figure 12. During this measurement, current is forced, while voltage is sensed. As shown schematically in the legend of Figure 12, the labels C1 – C4 indicate contacts were applied to the 4 corners of the sample, and current-voltage checks were performed in multiple pathways. The resistivity (ρ) and sheet resistivity (ρ_s) values from the 4P measurements were in the order of 13.6 - 15.5 Ω.cm and 4.5×10^7 - 5.2×10^7 $\Omega.sq^{-1}$ respectively. Discrepancies between these resistance values and those obtained via the colinear 4P measurements may be due to different electronic effects originating from the substrate. The colinear and Hall 4P measurements were obtained from MoS_2 deposited on SiO_2/Si and Al_2O_3 substrates, respectively. Notably, Ma et al. observed that the choice of encapsulating dielectric affects the charge transport in ultra-thin MoS_2.[46] Thus, the identity of the substrate is a likely culprit for the observed differences in resistivities.

The accuracy of the Hall 4P measurements is bolstered by an F-value of 0.99, where any F-value greater than 0.95 indicates the resemblance of the sample being measured with the ideal Van der Pauw structure, hence confirming the reliability of the measurements. AC measurements were presently unreliable due to poor signal-to-noise ratios, which is a known issue for ALD/CVD TMDC films,[47] and this is currently under further investigation.

Contrasting ρ measured here with values extracted from other TMDC thin-films, we note the value is consistent, in terms of being in a meaningful range for non-intentionally doped films. Measured on the same LakeShore system as in this work, the large data set in Lin et al.[47] demonstrated ρ in the 1.4-3.3 kΩ.cm range for MoS_2 CVD films, as a function of substrate and deposition temperature. Similarly, PtS from H_2S converted Pt, produced thin-films with ρ in the order of 318 Ω.cm,[48] while ALD WS_2 yielded a 4P ρ of 2 Ω.cm.[49] Lastly, using device test structures, ρ was observed to be 191 Ω.cm at room temperature in MoS_2 formed by thermal-assisted-conversion of Mo metal, decreasing to 41 Ω.cm when the measurement temperature was increased to 100 °C.[50]

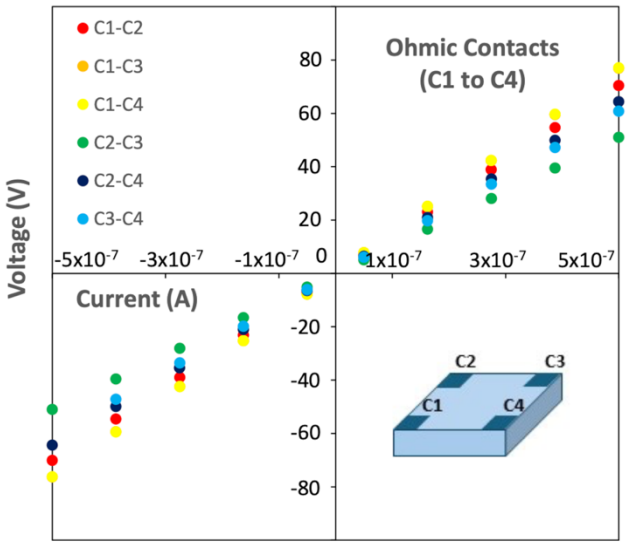

Figure 12. Representative current voltage characteristics taken from the Hall DC measurements performed on 1 cm × 1 cm MoS_2 (3 nm) samples deposited on sapphire, using TBDS as the precursor. During this measurement, current is forced, while voltage is sensed. The labels C1 – C4 indicate contacts were applied to the 4 corners of the sample, and current-voltage checks were performed in multiple pathways as indicated in the legend. The current voltage trend shows a linear characteristic through the origin.

Figure 13 shows representative current voltage characteristics taken from optical lithography defined circular test structures, where the MoS_2 thin-film was deposited on an SiO_2/Si substrate. The fabrication of these test structures has been described in previous work.[49] Evaluating the data

in terms of conductivity, the current-voltage trends show current scaling in accordance with voltage, inverse scaling with electrode separation, and exhibit a predominantly linear characteristic through the origin. All of these features indicate this MoS_2 thin-film shows promise for electron device operation and for nanoelectronic applications.

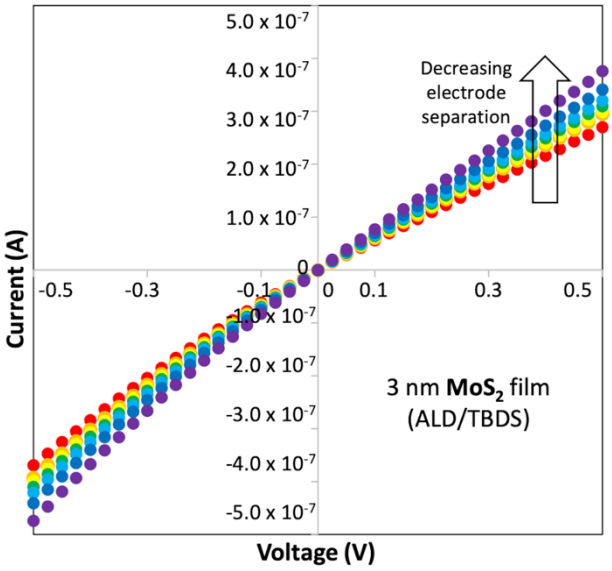

Figure 13. Representative current voltage characteristics taken from optical lithography defined circular test structures, where the MoS_2 thin-film is deposited on an SiO_2/Si substrate. Evaluating the data in terms of conductivity, the current-voltage trends show current scaling in accordance with voltage, inverse scaling with electrode separation, and exhibit a predominantly linear characteristic through the origin. All of these features indicate this MoS_2 thin-film shows promise for electron device operation and for nanoelectronic applications.

With respect to putting these data into perspective, the large dimensions of the test structures, or large spacings between probes is significant, especially when coupled with the nanometer scale of the thin-film thicknesses. As stated in our previous work,[15] this aspect ratio of channel length (electrode or probe spacing) versus film thickness is in the order of 10000:1 or more, which is extreme. The poly-crystalline nature of the films, along with the high surface to volume ratio, will undoubtedly hamper carrier transport due to scattering. A more favorable electrical evaluation will

come with scaled device dimensions to the sub-micron regime. Optimization of electron device performance will be the target of a future study.

CONCLUSIONS

We report a PEALD process that utilizes TBDS as an alternative sulfur precursor to H_2S for synthesizing layered MoS_2 thin films. The TBDS-based process has a slower growth rate compared to the H_2S-based process (1.1 vs 1.5 Å/cycle per AFM measurements), but it is capable of synthesizing stoichiometric MoS_2 with low carbon and nitrogen contamination at a deposition temperature of 350 °C. It was also found that the surface roughness of MoS_2 films synthesized using TBDS was more favorable for microelectronics applications than that observed for MoS_2 synthesized using H_2S. MoS_2 films synthesized with TBDS and H_2S were also found to have similar microstructure and electrical resistivity. Finally, Hall and C-TLM measurements demonstrate that the TBDS-based process is capable of preparing MoS_2 films for microelectronics applications, indicating that the TBDS-based ALD process herein is a suitable and relatively safe substitute for the H_2S-based process for low temperature, large area, layered MoS_2 deposition. Our findings suggest that the TBDS precursor can likely be applied in ALD processes for other layered transition metal chalcogenides.

ACKNOWLEDGEMENTS

This work has received funding from The Netherlands Organization for Scientific Research (NWO) through project 17846 “Defects, a curse or a blessing: tailoring defects in two-dimensional transition metal dichalcogenides by atomic layer deposition” and European Commission through

project ASCENT+: Access to European Infrastructure for Nano-electronics, funded under H2020, grant 871130.

This publication has also emanated from research supported in part by a grant from Science Foundation Ireland under Grant number 21/FFP-A/9897. AG, PM, AA, and RD thank Jun Lin and Brendan Sheehan at the Tyndall National Institute, for their advice and assistance during the Hall measurements and TEM analysis.

ASSOCIATED CONTENT

File contents: Additional experimental details, materials, methods and data, including specifics regarding the structure of ALD processes used in the manuscript and spectroscopic ellipsometry, Raman, atomic force microscopy, X-ray photoelectron spectroscopy, and transmission electron microscopy data (DOC).

AUTHOR INFORMATION

Corresponding Author

Ageeth Bol

Professor of Chemistry, Professor of Materials Science and Engineering

aabol@umich.edu

Author Contributions

The manuscript was written through contributions of all authors. All authors have given approval to the final version of the manuscript.

Funding Sources

This work has received funding from The Netherlands Organization for Scientific Research (NWO) through Vici project 17846 “Defects, a curse or a blessing: tailoring defects in two-dimensional transition metal dichalcogenides by atomic layer deposition” and European Commission through project ASCENT+: Access to European Infrastructure for Nano-electronics, funded under H2020, grant 871130.

This publication has also emanated from research supported in part by a grant from Science Foundation Ireland under Grant number 21/FFP-A/9897. AG, PM, AA, and RD thank Jun Lin and Brendan Sheehan at the Tyndall National Institute, for their advice and assistance during the Hall measurements and TEM analysis.

REFERENCES

1. Richey, N. E., De Paula, C. & Bent, S. F. Understanding chemical and physical mechanisms in atomic layer deposition. *Journal of Chemical Physics* **152**, 040902 (2020).
2. Fonseca, J. & Lu, J. Single-Atom Catalysts Designed and Prepared by the Atomic Layer Deposition Technique. *ACS Catal* **11**, 7018–7059 (2021).
3. Lu, J. A Perspective on New Opportunities in Atom-by-Atom Synthesis of Heterogeneous Catalysts Using Atomic Layer Deposition. *Catal Letters* **151**, 1535–1545 (2021).
4. Cremers, V., Puurunen, R. L. & Dendooven, J. Conformality in atomic layer deposition: Current status overview of analysis and modelling. *Appl Phys Rev* **6**, 021302 (2019).
5. Ahvenniemi, E. *et al.* Review Article: Recommended reading list of early publications on atomic layer deposition—Outcome of the “Virtual Project on the History of ALD”. *Journal of Vacuum Science & Technology A: Vacuum, Surfaces, and Films* **35**, 010801 (2017).
6. Parsons, G. N. *et al.* History of atomic layer deposition and its relationship with the American Vacuum Society. *Journal of Vacuum Science & Technology A: Vacuum, Surfaces, and Films* **31**, 050818 (2013).
7. Alvaro, E. & Yanguas-Gil, A. Characterizing the field of Atomic Layer Deposition: Authors, topics, and collaborations. *PLoS One* **13**, 1–19 (2018).
8. Sowa, M. The plasma enhanced atomic layer deposition publication database. https://www.plasma-ald.com/. (Accessed: 2024-05-14).
9. AtomicLimits, ALD database, doi:10.6100/alddatabase, 2020. https://www.atomiclimits.com/alddatabase/. (Accessed: 2024-05-14)

10. Mattinen, M., Leskelä, M. & Ritala, M. Atomic Layer Deposition of 2D Metal Dichalcogenides for Electronics, Catalysis, Energy Storage, and Beyond. *Adv Mater Interfaces* **8**, 1–47 (2021).
11. Lembke, D., Bertolazzi, S. & Kis, A. Single-Layer MoS 2 Electronics. *Acc Chem Res* **48,** 100-110 (2015).
12. Li, N. *et al.* Large-scale flexible and transparent electronics based on monolayer molybdenum disulfide field-effect transistors. *Nat Electron* **3**, 711–717 (2020).
13. Tang, J. *et al.* Low power flexible monolayer MoS2 integrated circuits. *Nat Commun* **14**, 1–8 (2023).
14. Sharma, A. *et al.* Low-temperature plasma-enhanced atomic layer deposition of 2-D MoS2: Large area, thickness control and tuneable morphology. *Nanoscale* **10**, 8615–8627 (2018).
15. Mattinen, M. *et al.* Atomic Layer Deposition of Large-Area Polycrystalline Transition Metal Dichalcogenides from 100 °C through Control of Plasma Chemistry. *Chemistry of Materials* **34**, 7280–7292 (2022).
16. Mughal, A. J., Walter, T. N., Cooley, K. A., Bertuch, A. & Mohney, S. E. Effect of substrate on the growth and properties of MoS2 thin films grown by plasma-enhanced atomic layer deposition. *Journal of Vacuum Science & Technology A: Vacuum, Surfaces, and Films* **37**, 010907 (2019).
17. Tan, L. K. *et al.* Atomic layer deposition of a MoS2 film. *Nanoscale* **6**, 10584–10588 (2014).
18. Nandi, D. K., Sen, U. K., Choudhury, D., Mitra, S. & Sarkar, S. K. Atomic layer deposited MoS2 as a carbon and binder free anode in Li-ion battery. *Electrochim Acta* **146**, 706–713 (2014).
19. Mattinen, M. *et al.* Atomic Layer Deposition of Crystalline MoS2 Thin Films: New Molybdenum Precursor for Low-Temperature Film Growth. *Adv Mater Interfaces* **4**, 1700123 (2017).
20. Jurca, T. *et al.* Low-Temperature Atomic Layer Deposition of MoS 2 Films. *Angewandte Chemie* **129**, 5073–5077 (2017).
21. Hydrogen Sulfide. *Occupational Health and Safety Administration* https://www.osha.gov/hydrogen-sulfide/hazards. (Accessed: May 14, 2024)
22. Guidotti, T. L. Hydrogen sulfide: Advances in understanding human toxicity. *Int J Toxicol* **29**, 569–581 (2010).
23. Batterman, S., Grant-Alfieri, A. & Seo, S. H. Low level exposure to hydrogen sulfide: a review of emissions, community exposure, health effects, and exposure guidelines. *Crit Rev Toxicol* **53**, 244–295 (2023).
24. Shen, C. *et al.* Morphology-controlled MoS2by low-temperature atomic layer deposition. *Nanoscale* **12**, 20404–20412 (2020).
25. Sopha, H. *et al.* ALD growth of MoS2 nanosheets on TiO2 nanotube supports. *FlatChem* **17**, 100130 (2019).
26. Yaws, C. L. & Satyro, M. A. Vapor Pressure – Organic Compounds. in *The Yaws Handbook of Vapor Pressure* (2015). doi:10.1021/ja01653a054.
27. Li, H. *et al.* Organosulfur precursor for atomic layer deposition of high-quality metal sulfide films. *Chemistry of Materials* **32**, 8885–8894 (2020).
28. Liu, H. *et al.* Atomic layer deposited 2D MoS2 atomic crystals: from material to circuit. *Nano Res* **13**, 1644–1650 (2020).

29. Zhang, T. *et al.* High performance few-layer MoS2 transistor arrays with wafer level homogeneity integrated by atomic layer deposition. *2d Mater* **5**, 015028 (2018).
30. Cadot, S. *et al.* A novel 2-step ALD route to ultra-thin MoS2 films on SiO2 through a surface organometallic intermediate. *Nanoscale* **9**, 538–546 (2017).
31. Kalanyan, B. *et al.* MoS2 thin films from a (N t Bu)2(NMe2)2Mo and 1-propanethiol atomic layer deposition process . *Journal of Vacuum Science & Technology A: Vacuum, Surfaces, and Films* **37**, 010901 (2019).
32. Jin, Z., Shin, S., Kwon, D. H., Han, S. J. & Min, Y. S. Novel chemical route for atomic layer deposition of MoS2 thin film on SiO2/Si substrate. *Nanoscale* **6**, 14453–14458 (2014).
33. Jeon, W., Cho, Y., Jo, S., Ahn, J. H. & Jeong, S. J. Wafer-Scale Synthesis of Reliable High-Mobility Molybdenum Disulfide Thin Films via Inhibitor-Utilizing Atomic Layer Deposition. *Advanced Materials* **29**, 1703031 (2017).
34. Mignuzzi, S. *et al.* Effect of disorder on Raman scattering of single-layer Mo S2. *Phys Rev B Condens Matter Mater Phys* **91**, 1–7 (2015).
35. Li, H. *et al.* From bulk to monolayer MoS 2: Evolution of Raman scattering. *Adv Funct Mater* **22**, 1385–1390 (2012).
36. Chakraborty, B., Matte, H. S. S. R., Sood, A. K. & Rao, C. N. R. Layer-dependent resonant Raman scattering of a few layer MoS2. *Journal of Raman Spectroscopy* **44**, 92–96 (2013).
37. Jeon, J. *et al.* Layer-controlled CVD growth of large-area two-dimensional MoS2 films. *Nanoscale* **7**, 1688–1695 (2015).
38. Rice, C. *et al.* Raman-scattering measurements and first-principles calculations of strain-induced phonon shifts in monolayer MoS2. *Phys Rev B Condens Matter Mater Phys* **87**, 081307 (2013).
39. Bertuch, A., Keller, B. D., Ferralis, N., Grossman, J. C. & Sundaram, G. Plasma enhanced atomic layer deposition of molybdenum carbide and nitride with bis(tert -butylimido)bis(dimethylamido) molybdenum . *Journal of Vacuum Science & Technology A: Vacuum, Surfaces, and Films* **35**, 01B141 (2017).
40. Molina, A., Campbell, I. E., Walter, T. N., Agyapong, A. D. & Mohney, S. E. Molybdenum carbonitride deposited by plasma atomic layer deposition as a Schottky contact to gallium nitride. *Appl Phys Lett* **119**, 102102 (2021).
41. Naumkin, A. V., Kraut-Vass, A., Gaarenstroom, S. W. & Powell, C. J. NIST X-ray Photoelectron Spectroscopy Database. *National Institute of Standard and Technology* https://srdata.nist.gov/xps/ (Accessed: 2024-05-14).
42. Baker, M. A., Gilmore, R., Lenardi, C. & Gissler, W. XPS investigation of preferential sputtering of S from MoS2 and determination of MoSx stoichiometry from Mo and S peak positions. *Appl Surf Sci* **150**, 255–262 (1999).
43. Greczynski, G. & Hultman, L. A step-by-step guide to perform x-ray photoelectron spectroscopy. *J Appl Phys* **132**, 011101 (2022).
44. Samaniego-Benitez, J. E. *et al.* Synthesis and structural characterization of MoS2 micropyramids. *J Mater Sci* **55**, 12203–12213 (2020).
45. Tan, L. K. *et al.* Atomic layer deposition of a MoS2 film. *Nanoscale* **6**, 10584–10588 (2014).
46. Ma, N. & Jena, D. Charge scattering and mobility in atomically thin semiconductors. *Phys Rev X* **4**, 011043 (2014).

47. Lin, J. *et al.* Large-area growth of MoS2at temperatures compatible with integrating back-end-of-line functionality. *2d Mater* **8**, 025008 (2021).
48. Monaghan, S. *et al.* Structural and electrical characterisation of PtS from H2S-converted Pt. *Appl Mater Today* **25**, 101163 (2021).
49. Coleman, E. *et al.* Scrutinizing pre- and post-device fabrication properties of atomic layer deposition WS2 thin films. *Appl Phys Lett* **123**, 011901 (2023).
50. Duffy, R. *et al.* Structural and Electrical Investigation of MoS 2 Thin Films Formed by Thermal Assisted Conversion of Mo Metal . *ECS Journal of Solid State Science and Technology* **5**, Q3016–Q3020 (2016).

For Table of Contents Only